

Highly responsive photodetectors based on $NiPS_3/WS_2$ van der Waals type-II heterostructures

Zhiteng Li(李志腾), Ian Wang(王易安), Zhenming Qiu(邱振铭), Lin Wang(王琳), Xiaofeng Liu(刘小峰), Zhengwei Chen(陈政委), and Xiao Zhang(张晓)

Citation: Chin. Phys. B, 2025, 34 (**2**): 027201. DOI: 10.1088/1674-1056/ad9e97
Journal homepage: http://cpb.iphy.ac.cn; http://iopscience.iop.org/cpb

What follows is a list of articles you may be interested in

Temperature dependence on the electrical and physical performance of InAs/AlSb heterojunction and high electron mobility transistors

Jing Zhang(张静), Hongliang Lv(吕红亮), Haiqiao Ni(倪海桥), Zhichuan Niu(牛智川), Yuming Zhang(张玉明)
Chin. Phys. B, 2018, 27 (**9**): 097201. DOI: 10.1088/1674-1056/27/9/097201

Room-temperature operating extended short wavelength infrared photodetector based on interband transition of InAsSb/GaSb quantum well

Ling Sun(孙令), Lu Wang(王禄), Jin-Lei Lu(鲁金蕾), Jie Liu(刘洁), Jun Fang(方俊), Li-Li Xie(谢莉莉), Zhi-Biao Hao(郝智彪), Hai-Qiang Jia(贾海强), Wen-Xin Wang(王文新), Hong Chen(陈弘)
Chin. Phys. B, 2018, 27 (**4**): 047209. DOI: 10.1088/1674-1056/27/4/047209

Spectral response modeling and analysis of p-n-p $In0.53Ga_{0.47}As/InP$ HPTs

Jun Chen(陈俊), Jiabing Lv(吕加兵)
Chin. Phys. B, 2016, 25 (**9**): 097202. DOI: 10.1088/1674-1056/25/9/097202

Photoactive area modification in bulk heterojunctionorganic solar cells using optimization of electrochemicallysynthesized ZnO nanorods

Mehdi Ahmadi, Sajjad Rashidi Dafeh
Chin. Phys. B, 2015, 24 (**11**): 117203. DOI: 10.1088/1674-1056/24/11/117203

Effect of charge order transition on tunneling resistance in $Pr_{0.6}Ca_{0.4}MnO_3$/Nb-doped $SrTiO_3$ heterojunction

Wang Deng-Jing (王登京), Ma Jun-Jie (马俊杰), Wang Mei (王妹), Wang Ru-Wu (汪汝武), Li Yun-Bao (李云宝)
Chin. Phys. B, 2014, 23 (**5**): 057202. DOI: 10.1088/1674-1056/23/5/057202

Highly responsive photodetectors based on $NiPS_3/WS_2$ van der Waals type-II heterostructures

Zhiteng Li(李志腾)[1], Yian Wang(王易安)[2], Zhenming Qiu(邱振铭)[1], Lin Wang(王琳)[3], Xiaofeng Liu(刘小峰)[3], Zhengwei Chen(陈政委)[1,†], and Xiao Zhang(张晓)[1,‡]

[1] *State Key Laboratory of Information Photonics and Optical Communications & School of Science, Beijing University of Posts and Telecommunications, Beijing* 100876, *China*

[2] *The High School Affiliated to Renmin University of China, Beijing* 100080, *China*

[3] *School of Materials Science and Engineering, Zhejiang University, Hangzhou* 310027, *China*

(Received 15 September 2024; revised manuscript received 19 November 2024; accepted manuscript online 13 December 2024)

A heterostructure photodetector composed of few-layer $NiPS_3/WS_2$ is made by using mechanical exfoliation and micro-nano fabrication techniques. The photodetector exhibits a broad-band response wavelengths of ranging of 405 nm and 800 nm. Under the light illumination of 405-nm wavelength and a bias voltage of −2 V, the photoresponsivity is 62.6 mA/W and the specific detectivity is 8.59×10^{10} Jones. In addition, the device demonstrates a relatively fast response with rise and fall times of 70 ms and 120 ms. Theoretical calculation suggest that this excellent performance can be ascribed to the type-II band alignment at the $NiPS_3/WS_2$ heterostructure interface.

Keywords: heterojunction, photodetector, $NiPS_3$, WS_2

PACS: 72.40.+w, 68.37.–d, 79.60.Jv, 73.20.At

DOI: 10.1088/1674-1056/ad9e97 **CSTR:** 32038.14.CPB.ad9e97

1. Introduction

With the rapid development of the microelectronics industry, the integration of devices in integrated circuits is increasingly approaching the physical limit of Moore's law. The search for new semiconducting materials and the development of new design processes are becoming important.[1] Two-dimensional (2D) materials, with their ultra-thin structure, atomically flat ideal interfaces, flexible stacking characteristics, and high carrier mobility, provide a key material platform for the development of miniaturized optoelectronic devices.[2–4] The transition metal dichalcogenides (TMDCs) with semiconducting properties have attracted intensive attention due to their excellent optical electronic properties and thickness-tunable bandgap.[5] However, TMDCs have optical bandgaps in the range of 0.8 eV–2.1 eV. The relatively small bandgap limits its application in the field of ultraviolet detection.

Recently, a new class of van der Waals (vdW) materials transition metal phosphorus sulfides (TMPSs) with the general formula MPX_3 (M = Mn, Fe, Ni; X = S, Se) have discovered.[6–10] The TMPSs show semiconducting behaviors with relatively large bandgaps (1.3 eV–3.5 eV) and can be easily exfoliated down to few nanometers, thus they become a novel platform for ultraviolet and broad-band detection.[11] Owing to their weak interlayer vdW interactions, TMPSs and TMDCs can be combined together to construct high-efficiency, wide-spectrum optoelectronic heterostructure devices.[12] Among TMPSs, $NiPS_3$ has a direct optical gap of ∼ 1.402 eV and it shows a promising potential for use in photoelectric detection due to its thickness-tunable bandgap and air stability.[13] Moreover, field-effect transistors (FETs) based on few-layer $NiPS_3$ has been produced, Chu *et al*. have used few-layer $NiPS_3$ to make ultraviolet photodetectors, exhibiting good photoelectric performance.[14] Zong *et al*. have designed asymmetric electrode contacts, making the Schottky barriers of the two electrode contacts unbalanced, thus making the device show zero-bias photoelectric response.[15] However, the external quantum efficiency (EQE) of these devices is not high, i.e., fewer incident photons are effectively converted into current, which will affect their performance of practical application.

Because the formation of heterostructures can effectively prevent the recombination of electrons and holes, and thus improving the responsivity (R), thereby improve the EQE,[16] we fabricated $NiPS_3/WS_2$ heterostructure photodetectors, which exhibited a broad-band response, high photo-responsivity, and specific detectivity, particularly under 405-nm light. This superior performance may be attributed to the type-II band alignment at the $NiPS_3/WS_2$ interface.

†Corresponding author. E-mail: qq619755720@bupt.edu.cn

‡Corresponding author. E-mail: zhangxiaobupt@bupt.edu.cn

© 2025 Chinese Physical Society and IOP Publishing Ltd. All rights, including for text and data mining, AI training, and similar technologies, are reserved.

2. Results and discussion

Figure 1(a) presents the schematic diagrams of the crystal structures of monolayer $NiPS_3$ and WS_2 and their heterostructure. $NiPS_3$ belongs to the $C2/m$ space group and the layers are connected by weak vdW forces. The unit cell of WS_2 has a unit cell composed of one tungsten atom and two sulfur atoms in a trigonal prismatic configuration, belonging to the $P6_3/mmc$ space group. Each layer is fixed together by vdW forces as well. Figure 1(b) shows an optical microscope image of the heterostructure photodetector composed of few-layer $NiPS_3$ and WS_2. The heterostructure are formed by overlapping $NiPS_3$ and WS_2 on SiO_2/Si substrate and the area of the heterostructure is about 654 μm^2. The lower right part of Fig. 1(b) displays the atomic force microscopy (AFM) image of the rectangular area in the optical microscope, and the thicknesses of the two samples measured along the white lines are shown in Fig. 1(c). The thickness of $NiPS_3$ and WS_2 is about 23 nm and 18 nm, respectively. Figure 1(d) presents the Raman spectra of few-layer $NiPS_3$, WS_2, and $NiPS_3/WS_2$ heterostructures. The peak at 253 cm^{-1} corresponds to the $A_{1g}^{(1)}$ vibrational mode caused by the in-plane vibration of S atom in $NiPS_3$ and the peaks at 382 cm^{-1} and 582 cm^{-1} correspond to the $A_{1g}^{(2)}$ and $A_{1g}^{(3)}$ vibrational modes, caused by the vertical vibration of S atom. The peaks at 130 cm^{-1}, 176 cm^{-1}, 279 cm^{-1}, and 559 cm^{-1} correspond to the $E_g^{(1)}$, $E_g^{(2)}$, $E_g^{(4)}$ and $E_g^{(5)}$ vibrational modes, which are related to the vibration modes of Ni atom. On the other hand, the two characteristic Raman peaks of few-layer WS_2 are 351 cm^{-1} and 420 cm^{-1} correspond to the $E_{2g}^{(1)}$ and $A_{1g}^{(2)}$ vibrational modes. As shown in the bottom of Fig. 1(d), the characteristic peaks of both $NiPS_3$ and WS_2, can be observed $NiPS_3/WS_2$ overlapping area, confirming the formation of heterostructure.

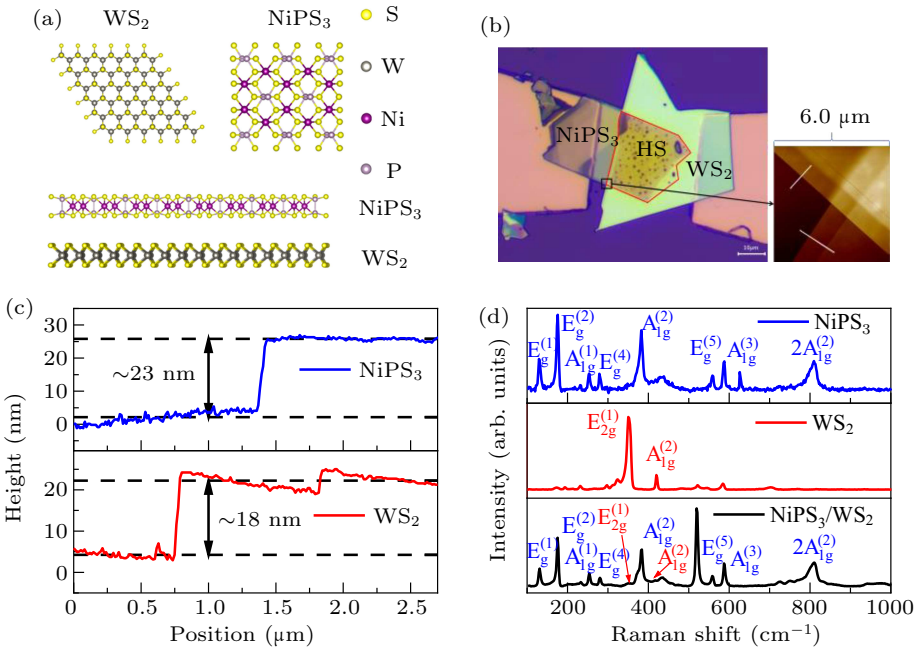


Fig. 1. (a) Crystal structures of monolayer WS_2, $NiPS_3$, and $NiPS_3/WS_2$. (b) Left: optical microscope image of the $NiPS_3/WS_2$ photodetector. Right: AFM image of $NiPS_3/WS_2$ around 6.0 μm×6.0 μm. (c) Height profile along the white lines in the AFM image of the sample shown in panel (b). (d) Raman spectra of $NiPS_3$, WS_2, and heterostructure.

Figure 2(a) presents a schematic diagram of $NiPS_3/WS_2$ heterostructure photodetector. From bottom to top, the detector is composed of SiO_2/Si substrate, Ti/Au electrodes, WS_2, and $NiPS_3$ with a gold electrode spacing of ∼ 40 μm. Figure 2(b) show the drain–source current–voltage (I_{ds}–V_{ds}) characteristic curves of $NiPS_3/WS_2$ heterostructure with different laser wavelengths (the diameter of the laser spot is ∼ 77 μm). When the heterostructure is illuminated under the light of different wavelengths, significant changes of I_{ds} can be observed in Fig. 2(b). Among them, the photocurrent generated under the condition of −2-V bias and 405-nm light is the largest and the current rises from the dark state of 5.2×10^{-13} A to 2.6×10^{-9} A. Such a significant change indicates the generation of a large number of electron–hole pairs under illumination. As the illumination condition changes from the dark state to 405-nm illumination, the open-circuit voltage (V_{oc}) changes from 0 V in the dark state to 0.23 V and the short-circuit current (I_{sc}) raises to 1.67×10^{-10} A (Fig. 2(c)), showing a significant photoelectric effect. At the same time, the I_{ds}–V_{ds} characteristic curves under different powers with a wavelength of 405 nm have also been measured (see Fig. S1 in the supporting information). On the one hand, the photocurrent significantly increases with light power at $V_{ds} = 0$ V, it suggests that photo-generated carriers are efficiently separated and driven

by an internal electric field. On the other hand, the increase of V_{oc} with increasing light power can also indicate the presence of strong internal electric field. The above results indicate that a strong built-in electric field E_{in} has been formed in the $NiPS_3/WS_2$ heterostructure. In order to confirm the optoelectronic response is mainly induced by the heterojunction not the Schottky junction effect, scanning photocurrent mapping is used to acquire the photocurrent distribution (Fig. S2). It can be clearly seen that the photocurrent is mainly observed in the whole heterojunction area and no obvious current is generated near the metal contacts, which unambiguously demonstrates the photovoltaic current indeed originates from the heterojunction.

Figure 2(d) shows the switching response of the $NiPS_3/WS_2$ heterostructure over time under light illuminations with different wavelengths. The device exhibits a fast switching effect at different wavelengths, indicating that it can be easily adjusted. Moreover, the heterostructure still has a significant photoresponse without applying additional bias voltage, indicating its self-powered phenomenon, which is modulated by the photoelectric effect. To determine the specific rise and fall times of the device, the response of photodetector is characterized by amplifying the photoelectric response using a preamplifier and collecting the resulting voltage data with an oscilloscope. The rise and fall time refer to the time required for the stable current value to go from 10% to 90% and from 90% to 10%, respectively. However, since only the voltage data is collected, the rise and fall times can be seen as the time required for the stable voltage value to go from 10% to 90% and from 90% to 10%, respectively. As depicted in Fig. S3, under zero-bias and illumination of 405-nm light with power density of 30 mW/cm^2, the rise and fall time is 70 ms and 120 ms, respectively, indicating that the photogenerated electron–hole pairs quickly separate under the effect of the E_{in}.

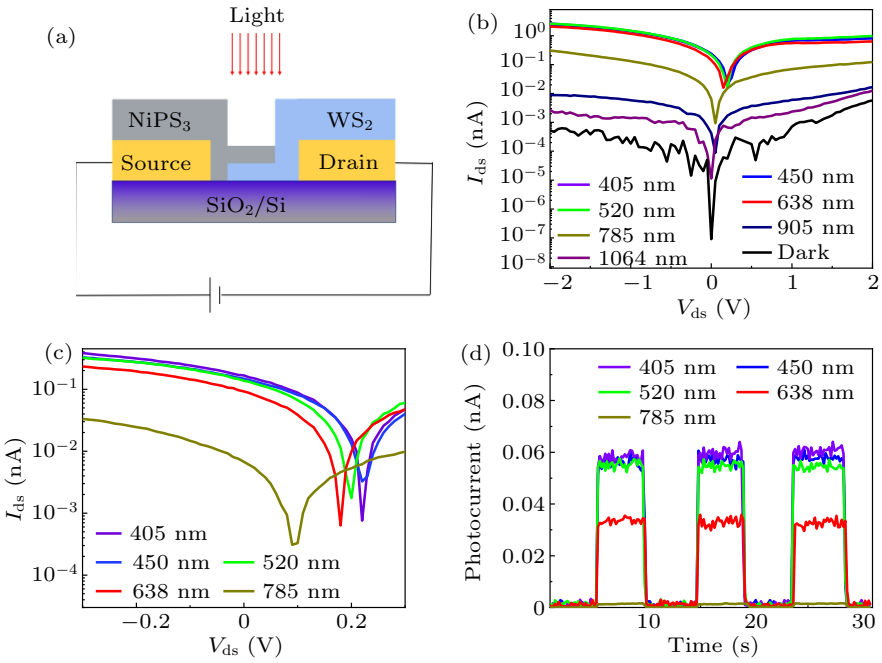


Fig. 2. (a) Schematic diagram of the $NiPS_3/WS_2$ photodetector. (b) I_{ds}–V_{ds} curves with various laser wavelengths at a power density of 50 mW/cm^2. (c) The enlarged view of I_{ds}–V_{ds} curves in the range of $V_{ds} = -0.3$ V and 0.3 V. (d) Time-dependent photocurrent at zero bias with power density of 50 mW/cm^2.

Figure 3(a) shows the relationship between the photocurrent (I_{ph}) and the incident light power (P_{in}) at 0 V and -2 V biases. Here, the incident light wavelength is 405 nm, and the power density ranges from 1 mW/cm^2 to 300 mW/cm^2. The linear dependence of photocurrent on P_{in} in log-scale plot reflects $I_{ph} \propto P^{\alpha}$. The fitted α is 0.58 and 0.45 for $V_{ds} = 0$ and -2 V, which are less than 1. This may be due to the presence of some impurities or defects in the heterostructure. Some photogenerated carriers recombined with them, resulting in not all carriers participating in the conductive process.[17] Figure 3(b) shows the dependence of V_{oc} and I_{sc} on P_{in} under 405-nm illumination. The V_{oc} increases with the increase of P_{in}, indicating that a built-in electric field is formed in the heterostructure, and there is a significant photoelectric effect. At the same time, the I_{sc} also increases with P_{in} and the maximum value of I_{sc} is approximately 3.4×10^{-10} A when the light power density is 300 mW/cm^2.

The R and EQE are key parameters for evaluating photodetectors. Figure 3(c) depicts the variation of R and EQE with incident light power at a bias of -2 V. The R of the pho-

todetector is calculated according to $R = I_{ph}/P_{in}$. The EQE is calculated through EQE $= hc/\lambda e \times R \times 100\%$, where h is Planck's constant, e is the elementary charge, c is the speed of light, λ is the wavelength. Under a bias of -2 V and 405-nm illumination with $P_{in} = 1$ mW/cm^2, the calculated R has reached 62.6 mA/W and the EQE is 105.06%, higher than 100%. It indicates that photo-generated electrons and holes repeatedly flow into the circuit before recombination. Additionally, as the power increases, both the R and EQE decrease. At high power densities, a large number of electron–hole pairs are generated. However, the rate of carrier recombination can increase as more carriers are generated, leading to a saturation in photocurrent and causing the R and EQE to decrease. In addition, high light power can lead to a higher density of photo-generated carriers, which can fill trap states within the material. Once these traps are filled, additional carriers are more likely to recombine rather than contribute to the photocurrent. This recombination reduces the effective carrier collection, leading to lower R and EQE.[18]

Specific detectivity (D^*) is another key parameter of photodetectors, which is mainly influenced by the current noise, which is primarily composed of $1/f$ noise, shot noise, and thermal noise. The $1/f$ noise can be ignored at high detection frequencies. When a low bias is applied, the dark current of the heterojunction is relatively small. As a consequence, the contribution of shot noise can also be neglected, only leaving thermal noise to be considered. At this point, the D^* can be calculated according to $D^* = R/(R'A/4k_BT)^{1/2}$, where R' refers to the bias resistance, A is the effective area of the device, k_B is Boltzmann constant and T is temperature.[19] Figure 3(d) shows the changes of R and D^* with varying wavelengths under a bias of -2 V and $P_{in} = 1$ mW/cm^2. The results under 0-V and 2-V biases are shown in Fig. S4. It can be observed that the trends of D^* and R curves are similar at different biases. The D^* reaches the maximum value of 8.59×10^{10} Jones under 405-nm illumination and becomes very small when $\lambda > 800$ nm. It indicates that the $NiPS_3/WS_2$ heterostructure photodetector has broad-band absorption characteristics within the range of 405 nm–800 nm wavelength and possesses high R, EQE, and D^*. The I_{ds}–V_{ds} curves of $NiPS_3$ and WS_2 photodetector are shown in Fig. S5 and Table 1 presents a comparison of the performance of $NiPS_3$, WS_2, $NiPS_3/WS_2$ heterostructure, and several other photodetectors. It can be seen that the $NiPS_3/WS_2$ heterostructure exhibits better photodetection performance than single $NiPS_3$ or WS_2 photodetector.

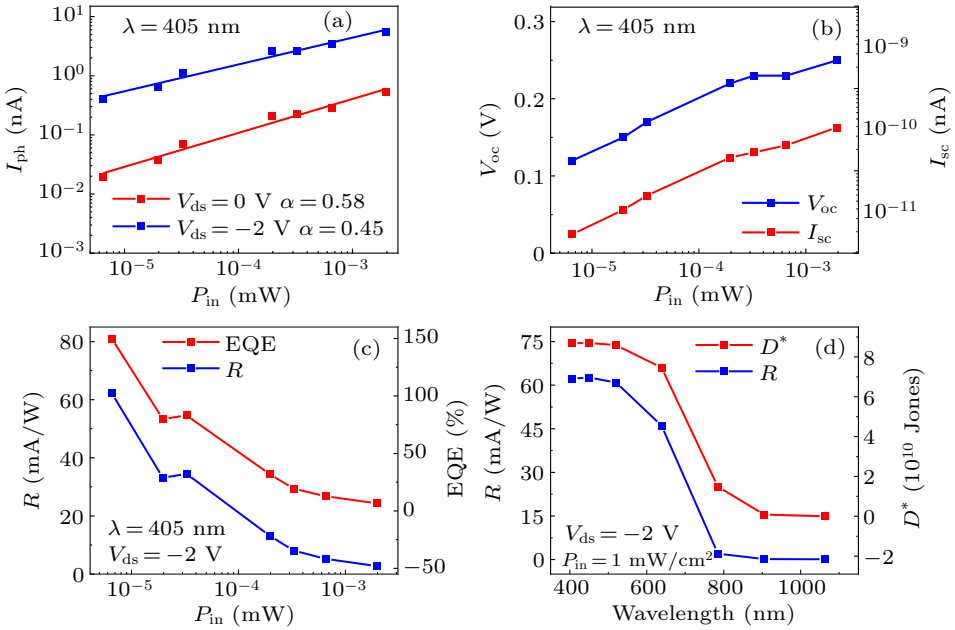


Fig. 3. (a) The relationship between I_{ph} and light power for the $NiPS_3/WS_2$ heterojunction. (b) The variation of V_{oc} and I_{sc} with incident light power. (c) The value of R and EQE with the increase of incident light power. (d) The variation of R and D^* with incident light wavelength.

Table 1. Performance of different photodetectors.

Materials	λ (nm)	V_{ds} (V)	P (mW/cm^2)	R (mA/W)	EQE	D^* (Jones)	Ref.
$NiPS_3/WS_2$	405	−2	1	62.6	105.06	8.59×10^{10}	this work
WS_2	405	2	30	18.02	43.45	1.25×10^{9}	this work
$NiPS_3$	405	2	30	0.76	1.83	3.85×10^{9}	this work
PtS_2/WS_2	635	0	0.0007	330	65.3	4.3×10^{10}	[20]
$FePS_3/WS_2$	450	−2	30	28.4	78.4	–	[17]
$MoSe_2/FePS_3$	600	0	30	52	12	1.4×10^{10}	[12]

In order to understand the optoelectronic properties of $NiPS_3/WS_2$ heterostructure further, we measured the band gap E_gs of $NiPS_3$ and WS_2 using absorption spectra and carried out the theoretical calculations. The estimated band gaps of $NiPS_3$ and WS_2 are ~ 2.07 eV and 1.56 eV (Figs. 4(a) and 4(b)) according to the formula $(\alpha h\nu)^2 = B(h\nu - E_g)$, where α is the absorption coefficient, h is Planck's constant, ν is the frequency, and B is a constant.[21] Furthermore, we use the core-level band alignment scheme[22] to obtain the energy states of $NiPS_3$ and WS_2 before contact. The core level energies are obtained by means of first-principles calculations. The energy difference between the Ni 3p core level and the valence band minimum (VBM) in $NiPS_3$ reaches 63.81 eV, while in WS_2, the energy difference between the W 4f core level and the VBM is 28.94 eV. Combing with the E_g obtained from absorption spectra, the diagram of band alignment before contact is depicted in Fig. 4(c). It can be seen that the $NiPS_3/WS_2$ heterostructure exhibits a type-II band alignment. An E_{in} can form at the heterostructure interface from WS_2 to $NiPS_3$, with positive and negative charge centers accumulating on the WS_2 and $NiPS_3$ sides, respectively. This enables the band edges of WS_2 and $NiPS_3$ to bend upward and downward, respectively (Fig. 4(d)).

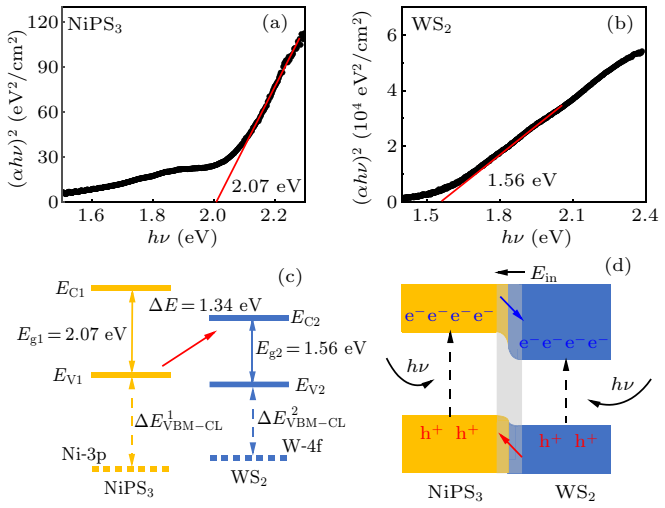


Fig. 4. The absorption spectra of (a) $NiPS_3$ and (b) WS_2. The red lines represent the linear fits to extract E_g. (c) The calculated band alignment diagrams of few-layer $NiPS_3$ and WS_2. (d) Schematic diagram of type-II band alignment of $NiPS_3/WS_2$ vdW heterostructure and carrier transport under illumination.

Under the zero bias, when illuminated by a laser, the electron–hole pairs are generated. These photo-generated electrons and holes are separated at the interface due to the E_{in}. When $V_{ds} > 0$, the forward bias reduces the strength of E_{in}, narrowing the depletion region. This reduction in the drift movement of photo-generated electrons and holes leads to an increased recombination rate of electron–hole pairs. Conversely, when $V_{ds} < 0$, the reverse bias increases the strength of E_{in}, widening the depletion region. The enhanced drift movement of carriers facilitates the passage of photo-generated carriers through E_{in}, thereby reducing the recombination rate and promoting rapid separation of photo-generated carriers. It is precisely the strong E_{in} and the type-II band alignment leading to the significantly reduced recombination rate of electrons and holes that result in superior optoelectronic performance of the $NiPS_3/WS_2$ heterostructure. Notably, previous studies of photoluminescence spectrum indicate that the band alignment of monolayer $NiPS_3/WS_2$ heterostructure is type-I,[23] which differs from our experimental results. This discrepancy might be due to the difference in material thickness. There are reports demonstrated that the E_gs of $NiPS_3$ and WS_2 are changed with different thicknesses,[24,25] thus the heterojunction may form different band alignments with different thicknesses. Similar situations have been observed in the study of $FePS_3/MoSe_2$ photodetectors.[12]

3. Conclusion

In summary, we prepared a few-layer $NiPS_3/WS_2$ heterostructure photodetector and studied its structure and optoelectronic properties in detail. The results show that the $NiPS_3/WS_2$ heterostructure photodetector has a characteristic of broad-band response of wavelengths of 400 nm to 800 nm. Under 405-nm illumination and $V_{ds} = -2$ V, the R is 62.6 mA/W and D^* is 8.59×10^{10} Jones. The performance of the heterostructure is superior to those of individual few-layer $NiPS_3$ and WS_2 photodetectors. Theoretical calculations suggest that the $NiPS_3/WS_2$ heterostructure interface forms a type-II band alignment structure, which facilitates the rapid separation of photo-generated electron–hole pairs and significantly shortens the response time, and thus leading to the excellent performance of the $NiPS_3/WS_2$ heterostructure. These findings suggest that $NiPS_3/WS_2$ heterostructures are promising candidates for high-performance, wide-spectrum photodetectors, with potential applications in advanced optoelectronic devices.

Supporting information

Device fabrication and measurement; I_{ds}–V_{ds} curves of the $NiPS_3/WS_2$ vdW heterostructure under 405-nm illumination with increasing powers; the rise and fall times of the heterostructure under a zero bias; the variation of responsivity and specific detectivity with incident light wavelength when $V_{ds} = 0$ V and 2 V; the I_{ds}–V_{ds} characteristic curves of WS_2 and $NiPS_3$ devices under illumination at different wavelengths are provided in supporting information.

Acknowledgements

Project supported by the National Key Research and Development Program of China (Grant No. 2022YFE0109200) and the National Natural Science Foundation of China (Grant Nos. 12074013 and 62175210).

References

[1] Lemme M C, Akinwande D, Huyghebaert C and Stampfer C 2022 *Nat. Commun.* **13** 1392
[2] Shanmugam V, Mensah R A, Babu K, Gawusu S, Chanda A, Tu Y, Neisiany R E, Försth M, Sas G and Das O 2022 *Part. Part. Syst. Charact.* **39** 2200031
[3] Ahmed A, Iqbal M Z, Dahshan A, Aftab S, Hegazy H H and Yousef E S 2024 *Nanoscale* **16** 2097
[4] Khan K, Tareen A K, Aslam M, Wang R, Zhang Y, Mahmood A, Ouyang Z, Zhang H and Guo Z 2020 *J. Mater. Chem. C* **8** 387
[5] Xie C, Mak C, Tao X and Yan F 2016 *Adv. Funct. Mater.* **27** 1603886
[6] Kim K, Lim S Y, Kim J, Lee J U, Lee S, Kim P, Park K, Son S, Park C H and Park J G 2019 *2D Mater.* **6** 041001
[7] Kumar R, Jenjeti R N, Austeria M P and Sampath S 2019 *J. Mater. Chem. C* **7** 324
[8] Gao Y, Lei S, Kang T, Fei L, Mak C L, Yuan J, Zhang M, Li S, Bao Q, Zeng Z, Wang Z, Gu H and Zhang K 2018 *Nanotechnology* **29** 244001
[9] Ahn E C 2020 *npj 2D Mater. Appl.* **4** 17
[10] Li H, Ruan S and Zeng Y 2019 *Adv. Mater.* **31** 1900065
[11] Du K Z, Wang X Z, Liu Y, Hu P, Utama M I B, Gan C K, Xiong Q and Kloc C 2016 *ACS Nano* **10** 1738
[12] Duan J, Chava P, Asl M G, Lu Y F, Erb D, Hu L, Echresh A, Rebohle L, Erbe A, Krasheninnikov A V, Helm M, Zeng Y J, Zhou S and Prucnal S 2022 *ACS Appl. Mater. Interfaces* **14** 11927
[13] Ho C H, Hsu T Y and Muhimmah L C 2021 *npj 2D Mater Appl.* **5** 8
[14] Chu J, Wang F, Yin L, Lei L, Yan C, Wang F, Wen Y, Wang Z, Jiang C, Feng L, Xiong J, Li Y and He J 2017 *Adv. Funct. Mater.* **27** 1701342
[15] Zong L, Song J, Wang S, Chen W, Yang J, Li B, Hu P, Fan H, Teng F and Zhao X 2023 *J. Mater. Chem. C* **12** 593
[16] Balapure A, Dutta J R and Ganesan R 2024 *RSC Appl. Interfaces* **1** 43
[17] Cao X, Yan S, Li Z, Fang Z, Wang L, Liu X, Chen Z, Lei H and Zhang X 2023 *J. Phys. Chem. Lett.* **14** 11529
[18] Zhao H, Yan Y, Song X, Ma Z, Tian T, Jiang Y, Li X, Xia C and Li J 2021 *Nanoscale* **13** 3757
[19] Chen Y, Wang Y, Wang Z, Gu Y, Ye Y, Chai X, Ye J, Chen Y, Xie R, Zhou Y, Hu Z, Li Q, Zhang L, Wang F, Wang P, Miao J, Wang J, Chen X, Lu W and Hu W 2021 *Nat. Electron.* **4** 357
[20] Wang Z, Zhang H, Wang W, Tan C, Chen J, Yin S, Zhang H, Zhu A, Li G, Du Y, Wang S, Liu F and Li L 2022 *ACS Appl. Mater. Interfaces* **14** 37926
[21] Tauc J, Grigorovici R and Vancu A 1966 *Phys. Status. Solidi B* **15** 627
[22] Kraut E A, Grant R W, Waldrop J R and Kowalczyk S P 1980 *Phys. Rev. Lett.* **44** 1620
[23] Tan Q, Luo W, Li T, Cao J, Kitadai H, Wang X and Ling X 2022 *Appl. Phys. Rev.* **9** 041406
[24] Hsu C, Frisenda R, Schmidt R, Arora A, de Vasconcellos S M, Bratschitsch R, van der Zant H S J and Castellanos-Gomez A 2019 *Adv. Opt. Mater.* **7** 1900239
[25] Lane C and Zhu J X 2020 *Phys. Rev. B* **102** 075124